



How inertial lift affects the dynamics of a microswimmer in Poiseuille flow

Akash Choudhary¹, Subhechchha Paul², Felix Rühle¹ & Holger Stark²

The transport of motile microorganisms is strongly influenced by fluid flows that are ubiquitous in biological environments. Here we demonstrate the impact of fluid inertia. We analyze the dynamics of a microswimmer in pressure-driven Poiseuille flow, where fluid inertia is small but non-negligible. Using perturbation theory and the reciprocal theorem, we show that in addition to the classical inertial lift of passive particles, the active nature generates a ‘swimming lift’, which we evaluate for neutral and pusher/puller-type swimmers. Accounting for fluid inertia engenders a rich spectrum of complex dynamics including bistable states, where tumbling coexists with stable centerline swimming or swinging. The dynamics is sensitive to the swimmer’s hydrodynamic signature and goes well beyond the findings at vanishing fluid inertia. Our work will have non-trivial implications on the transport and dispersion of active suspensions in microchannels.

¹Institute of Theoretical Physics, Technische Universität Berlin, 10623 Berlin, Germany. ²Department of Mechanical Engineering, Indian Institute of Engineering Science and Technology Shibpur, 711103 Shibpur, India. ✉email: a.choudhary@campus.tu-berlin.de; holger.stark@tu-berlin.de

Self-propelling microswimmers often experience dynamic fluid environments and confinements, for example, pathogens in lung mucus¹, microorganisms in laminar flow through porous matrix², and sperm cells in the Fallopian tubes³. Often these swimmers interact with micro-scale flows and boundaries⁴ to enhance survival probability⁵ and biofilm formation⁶ or cause intriguing collective patterns⁷. Their envisioned artificial counterparts—designed to execute *in vitro* drug delivery—also would have to interact with the dynamic conditions of such biological flows^{8,9}. Examining the dynamics of microswimmers can help us get insights into the dispersion of active suspensions¹⁰, it can also provide guidelines for the rational fabrication of microfluidic drug delivery and for minimizing biofilm formation in biomedical equipments¹¹.

Sheared flows in biological systems and microchannels impose substantial vorticity on the swimmer, which results in continuous tumbling. Past experimental and computational studies have shown that this tumbling, in conjunction with surface interactions, cause upstream swimming known as rheotaxis^{12–15}. Zöttl and Stark^{16,17} developed a theoretical model in the Stokes regime that captured swimming in Poiseuille flows. They reported upstream swinging and, for sufficiently strong flows, downstream tumbling states in planar and cylindrical channels. In two dimensions the phase portrait was found to be equivalent to that of a non-linear oscillator such as the pendulum. Related experimental and theoretical research studied single swimmer trajectories^{18,19}, shear-induced trapping²⁰, and focusing of phototactic algae²¹ or magnetotactic bacteria^{22,23}. Most recently, Peng and Brady¹⁰ investigated Taylor dispersion in active suspensions.

In recent years, experimental and theoretical studies have shown how inertia affects the unsteady propulsion of ciliated^{24,25} and larger swimmers^{26,27}. The influence of particle inertia has been discussed in refs. 28,29. With the recent advent of high-speed tunable microswimmers^{9,30,31}, understanding the effects of inertia can help in effective designs of biomedical devices. However, little is known how fluid inertia affects swimmer dynamics in sheared flows, which we will address in this article.

For passive particles, the Segré–Silberberg effect at finite Reynolds numbers has been known for decades^{32,33}. Inertial lift forces cause cross-stream migration and eventually focus particles roughly halfway between channel center and walls. This effect has initiated major advances in cell-sorting and flow cytometry techniques in the newly developing field of inertial microfluidics^{34,35}. To understand it, we note that a rigid particle resists the strain in background flow and generates a stresslet disturbance in the fluid decaying as $1/r^2$ ³⁶. The disturbance interacts with the curvature of the background flow and the channel walls, which in the presence of fluid inertia results in counter-acting shear-gradient and wall-induced lift forces that cause inertial focusing³⁷.

In his seminal work, Saffman³⁸ considered a particle moving relative to a uniform shear flow under the influence of an external (gravitational) force. He showed that it also experiences a cross-streamline lift. Similar investigations were presented in recent works on electrophoresis^{39–43}. They stressed the key role of the leading hydrodynamic multipole generated by the particle.

Microswimmers also move relative to an applied background flow. In this article, we consider the generic source–dipole and force–dipole microswimmers and calculate the resulting swimming lift in a planar Poiseuille flow when fluid inertia is small but non-negligible. We demonstrate that, in combination with the passive inertial lift, this gives rise to rich complex dynamics in channel flow, which goes well beyond the findings in refs. 16,17. Our work thereby opens up a new direction in the field of active

matter by connecting research on microswimmers to the field of inertial microfluidics with all its biomedical applications^{34,35}.

In the following, we consider a spherical swimmer of radius a that self-propels with velocity $\mathbf{v}_s = v_s \mathbf{p}$ in a two-dimensional Poiseuille flow $\mathbf{v}_f = v_m [1 - (x/w)^2] \mathbf{e}_z$ where v_m is the maximum flow velocity and w the half channel width (see Fig. 1). The overdamped motion of a noise-free swimmer can be described by dynamic equations for swimmer position (\mathbf{r}) and orientation (\mathbf{p}) vector,

$$\dot{\mathbf{r}} = \mathbf{p} + \bar{\mathbf{v}}_f + \mathcal{F}(x, \psi) \mathbf{e}_x, \quad \dot{\mathbf{p}} = \frac{1}{2} (\nabla \times \bar{\mathbf{v}}_f) \times \mathbf{p}, \quad (1)$$

where we rescaled velocities by swimming speed v_s , lengths by w , and time by w/v_s . \mathcal{F} denotes the total inertial lift velocity, which comprises the passive and swimming lift. It vanishes when fluid inertia becomes negligible and the system moves in the Stokesian regime as studied in ref. 16. The passive inertial lift is well-explored^{37,44,45} and, except in close vicinity to the channel walls, can be well approximated by $\mathcal{F}_{\text{passive}}(x) \approx \text{Re}_p \kappa \bar{v}_m x (1 - x^2/x_{\text{eq}}^2)$ (see “Methods” section). Here, x_{eq} denotes the stable equilibrium positions, $\kappa = a/2w$ the ratio of swimmer radius to channel width, and $\bar{v}_m = v_m/v_s$ is the scaled centerline flow velocity. The swimmer Reynolds number $\text{Re}_p = \rho v_m \kappa a / \mu$ is based on the characteristic shear around a swimmer; ρ and μ represent the fluid density and viscosity, respectively.

Results and discussion

Neutral swimmers. To evaluate the additional swimming lift $\mathcal{F}_{\text{swim}}$, we find the disturbance field \mathbf{v} created by the microswimmer using the continuity and the quasi-steady Navier–Stokes equations in the co-moving swimmer frame $\{\tilde{x}, \tilde{y}, \tilde{z}\}$,

$$\tilde{\nabla} \cdot \mathbf{v} = 0, \quad \text{Re}_p \mathbf{f} = \tilde{\nabla} \cdot \boldsymbol{\sigma}. \quad (2)$$

Here, $\mathbf{f} = \mathbf{v} \cdot \tilde{\nabla} \mathbf{v}_\infty + \mathbf{v}_\infty \cdot \tilde{\nabla} \mathbf{v} + \mathbf{v} \cdot \tilde{\nabla} \mathbf{v}$ results from the convective acceleration with \mathbf{v}_∞ the Poiseuille flow field in the swimmer frame, and $\boldsymbol{\sigma} = -p\mathbf{I} + 2\boldsymbol{\Theta}$ is the Newtonian stress tensor of the disturbance field, where p and $\boldsymbol{\Theta}$ represent pressure and the rate-of-strain tensor, respectively. First, we consider a neutrally buoyant microswimmer that generates a source–dipole disturbance that, in leading order, resembles the flow field generated by some ciliated microswimmers⁴⁶ and active droplets^{47,48}. Before evaluating the inertial swimming lift, we will perform an order-of-magnitude analysis to predict its scaling for small Re_p . This will provide a fundamental understanding of how weak inertia affects swimmer motion.

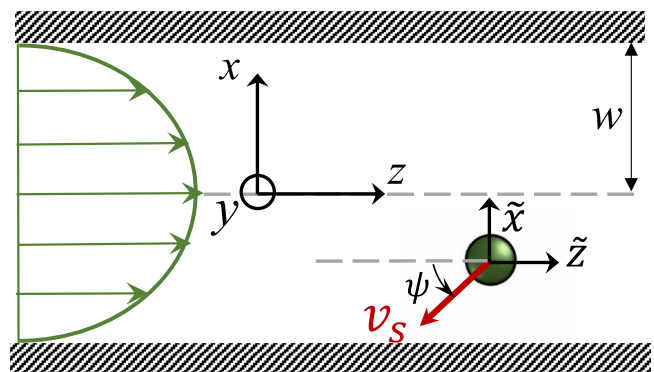


Fig. 1 A microswimmer in Poiseuille flow. A spherical microswimmer with velocity $v_s \mathbf{p}$ moves in a planar Poiseuille flow inside a channel with half width w . The coordinate frame $\{\tilde{x}, \tilde{y}, \tilde{z}\}$ co-moves with the swimmer.

The classical analyses of Oseen⁴⁹ and Saffman³⁸ demonstrated that the magnitude of inertial perturbations increases with distance from the swimmer until an asymptotic “cross-over radius”, beyond which the perturbations become singular. For the current swimmer system, the cross-over radius is $r_c \sim \text{Re}_p^{-1/238}$ that divides the entire domain in *inner* (regular) and *outer* (singular) regions. Substitution of r_c in the hydrodynamic signature of a neutral swimmer ($\sim 1/r^3$) suggests that singular lift is inferior to regular lift, i.e., $\mathcal{F}_{\text{swim}} \propto \text{Re}_p$ (see Supplementary Note 2). This is in contrast to the Saffman lift of a forced particle, where the singular contribution $\propto \text{Re}_p^{1/2}$ dominates. Hence, we implement a regular perturbation expansion, which turns the Navier–Stokes equations (2) into Stokes problems of zeroth ($\nabla \cdot \boldsymbol{\sigma}_0 = 0$) and first order ($\nabla \cdot \boldsymbol{\sigma}_1 = \mathbf{f}_0$), as detailed in the “Methods” section. Using the reciprocal theorem, we are able to calculate the swimming lift velocity from the first-order problem³⁷

$$\mathcal{F}_{\text{swim}} = -\frac{\text{Re}_p}{6\pi} \int_V \mathbf{v}^t \cdot \mathbf{f}_0 \, dV. \quad (3)$$

Here, the auxiliary velocity field \mathbf{v}^t belongs to a forced particle moving along the x -direction³⁷. The convective acceleration \mathbf{f}_0 corresponds to the Stokes solution \mathbf{v}_0 of the microswimmer consisting of a source-dipole field, which we adopt from the squirmer model^{50–52}, and a stresslet generated by the shearing background flow with rate-of-strain tensor \mathbf{e}_∞ ,

$$\mathbf{v}_0 = \frac{\tilde{v}_s \mathbf{p}}{2\tilde{r}^3} \cdot \left[\frac{3\tilde{r}\tilde{r}}{\tilde{r}^2} - \mathbf{1} \right] - \left[\frac{5\mathbf{e}_\infty : \tilde{r}\tilde{r}}{2\tilde{r}^5} \left(\tilde{r} - \frac{\tilde{r}}{\tilde{r}^2} \right) + \frac{\mathbf{e}_\infty \cdot \tilde{r}}{\tilde{r}^5} \right], \quad (4)$$

where $\tilde{v}_s = v_s/(v_m \kappa)$. We use here the far-field approximation to represent the flow field around microswimmers, which also strictly implies that the microswimmers should not come too close to the bounding walls. Using the corresponding \mathbf{f}_0 in Eq. 3 and \mathbf{e}_∞ for the Poiseuille flow, results in the inertial swimming lift velocity given in units of v_s : $\mathcal{F}_{\text{swim}} = -(7/6)\text{Re}_p x \cos \psi$. Thus, the total inertial lift to be used in Eq. 1 becomes

$$\mathcal{F} = \text{Re}_p \left[\kappa \bar{v}_m x \left(1 - \frac{x^2}{x_{\text{eq}}^2} \right) - x \cos \psi \right]. \quad (5)$$

where we skip the factor 7/6 for simplicity. We also calculated the modification to z -direction swimmer velocity and y -direction rotational velocity. The former is $-5/18\text{Re}_p x \sin \psi$ and latter is found to be identically zero at the present order of approximation.

The inertial lift profile of Eq. 5 causes a complex dynamics of the microswimmer governed by Eq. 1, which we now explore step by step. First of all, we identify two fixed points in the x – ψ plane at $x=0$, with the microswimmer either swimming upstream along the centerline ($\psi=0$) or downstream ($\psi=\pm\pi$). A linear stability analysis reveals the following approximate eigenvalues for these fixed points:

$$\begin{aligned} \lambda_1 &\approx \frac{\text{Re}_p}{2} (-1 + \kappa \bar{v}_m) \pm i \bar{v}_m^{1/2}, \\ \lambda_2 &\approx \frac{\text{Re}_p}{2} (1 + \kappa \bar{v}_m) \pm i \bar{v}_m^{1/2}. \end{aligned} \quad (6)$$

Downstream swimming corresponds to a saddle fixed point (λ_2), while upstream swimming along the centerline (λ_1) is stable for weak flows ($\bar{v}_m < \kappa^{-1}$) and unstable otherwise. The inertial lift profile plotted in Fig. 2 for a moderate flow strength and for different swimmer orientations ψ , shows the passive lift velocity at $\psi=\pi/2$ with an unstable position in the center and the two inertial focusing points at $\pm x_{\text{eq}}$. In the presence of the swimming

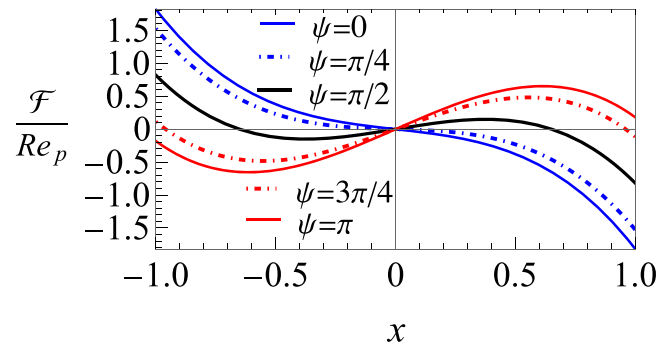


Fig. 2 Lift-velocity profile of a neutral swimmer. Inertial lift-velocity profiles of a source-dipole or neutral microswimmer for different orientation angles ψ for moderate flow speed $\bar{v}_m = 6$, $\kappa = 0.1$, and $x_{\text{eq}} = \pm 0.65$.

lift, the centerline position is stabilized at $\psi=0$. For strong flows ($\bar{v}_m > \kappa^{-1}$) the centerline position becomes unstable. However, the swimmer cannot focus on a non-zero x position, because due to the non-zero vorticity of the Poiseuille flow, it continuously tumbles while drifting downstream. In the state diagram presented in Fig. 3a, we vary swimmer size κ versus flow strength \bar{v}_m and find these two limiting cases in the lower left and upper right region, respectively. Around the dashed stability line, $\kappa = \bar{v}_m^{-1}$, we observe that fluid inertia engenders rich dynamics, which we discuss now.

We first look at smaller microswimmers with $\kappa \lesssim 0.1$ and move along the white dashed line in the state diagram with increasing \bar{v}_m . At $\bar{v}_m < 1$ the swimmer quickly reaches the centerline and moves upstream, while at moderate flow velocities $\bar{v}_m > 1$, it is drifted downstream by the Poiseuille flow and slowly relaxes towards the centerline (see Fig. 3b for a trajectory in x – z plane). On further increasing \bar{v}_m , a subcritical Hopf bifurcation occurs⁵³, where the stable centerline state and tumbling motion around x_{eq} coexist (see Fig. 3c). The schematic phase portrait in Fig. 3f shows how the stable fixed point and tumbling, a type of stable limit cycle, are separated by an unstable limit cycle. According to the bifurcation schematic next to the state diagram, the unstable limit cycle shrinks to zero and the fixed point becomes unstable. Hence, one observes a pure tumbling state (see Fig. 3d) with an amplitude that shrinks with increasing \bar{v}_m .

For larger microswimmers, we first concentrate on the white dashed line at $\kappa > 0.23$. When the fixed point becomes unstable at $\kappa = \bar{v}_m^{-1}$, a supercritical Hopf bifurcation occurs; the stable limit cycle, where the microswimmer performs a swinging motion about the centerline, gradually expands and then splits into two stable tumbling limit cycles. However, in the range $0.1 < \kappa < 0.23$ the swinging limit cycle first enters a small region where it coexists with the tumbling state (multiple limit cycles)⁵⁴ (see Fig. 3e). They are separated by an unstable limit cycle as the schematic phase portrait in Fig. 3g shows. As the flow rate further increases, the two inner limit cycles annihilate each other and the pure tumbling state remains.

In experiments, the time period of the swinging and tumbling states, as well as the drift velocity of the microswimmer along the channel axis, are measurable quantities. Figure 4a shows the time period T of the oscillatory states exhibited by the source-dipole swimmer for different rescaled swimmer sizes κ . At $\kappa = 0.15$, the two branches have an overlapping \bar{v}_m region. Here, swinging and tumbling states coexist as indicated in Fig. 3a and the swimmer state depends on the initial condition. Dashed lines indicate sharp transitions between the two states. As already observed in Fig. 3a, larger swimmers enter the oscillatory states at lower flow rates. In

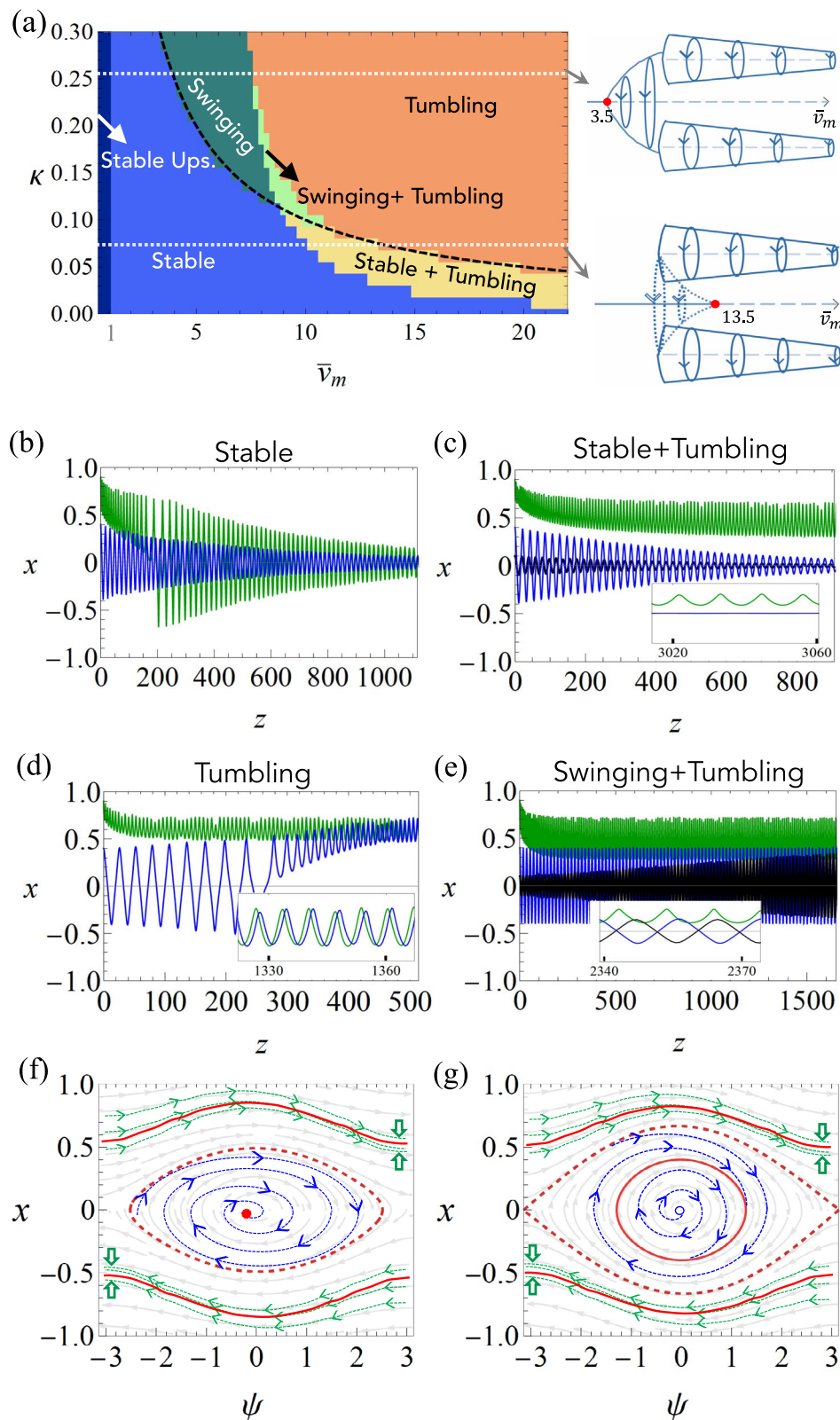


Fig. 3 Dynamics of a neutral microswimmer. **a** State diagram of a neutral microswimmer. To the left of the black dashed curve, $\kappa = \bar{v}_m^{-1}$, upstream-directed swimming along the centerline is stable. Along the white dashed lines at $\kappa = 0.25$ and $\kappa = 0.07$, the bifurcation characteristics are sketched on the right. Swimmer trajectories for different initial x positions [$x_0 = 0.9$ (green), $x_0 = 0.4$ (blue), $x_0 = 0.1$ (black)] and parameters: **b** $\bar{v}_m = 8, \kappa = 0.1$; **c** $\bar{v}_m = 11.5, \kappa = 0.05$; **d** $\bar{v}_m = 14, \kappa = 0.1$; **e** $\bar{v}_m = 9, \kappa = 0.125$. Other parameters are $\text{Re}_p = 0.1$, and $x_{\text{eq}} = \pm 0.65$. The insets show zoomed-in trajectories in steady state. **f, g** Schematic phase portraits for the trajectories in (c) and (e), respectively. The solid and dashed red lines depict stable and unstable limit cycles, respectively.

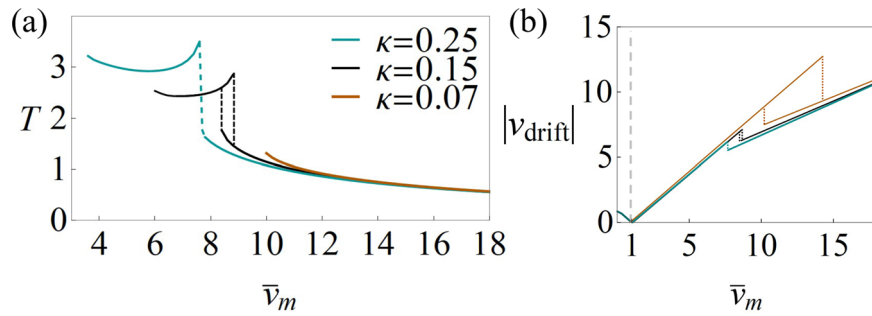


Fig. 4 Time period and drift speed. **a** Time period of swinging and tumbling motion and **b** drift speed along the channel axis plotted versus \bar{v}_m for different κ . The dashed lines indicate transitions between the two swimming states. Time period and drift speed are given in units of w/v_s and v_s , respectively.

the swinging state, we obtain a weak dependence of the time period on \bar{v}_m . Only close to the transition T rises with \bar{v}_m and then, in the tumbling state, it decreases slowly. Figure 4b shows that the drift speed along the channel axis rises linearly with \bar{v}_m with a slope one in the state of centerline swimming as expected. Also, in the swinging state ($\kappa = 0.15$ and 0.25) the slope is close to one. After the sharp drop to the tumbling state indicated by the dashed line, all three curves fall again nearly on top of each other. The slope of these straight lines is around 0.5, indicating that tumbling occurs outside of the centerline.

Pusher/puller-type swimmers. So far we have concentrated on microswimmers that generate a source–dipole flow field. Since the swimming lift crucially depends on the swimmer’s hydrodynamic signature and thus on its propulsion mechanism, we also expect a fundamentally distinct dynamics. Microswimmers that self-propel by rotating or beating flagella, such as *E. coli* and *Chlamydomonas*, generate a force–dipole flow field at the leading order^{55,56}. $\mathbf{v}_0 = \mathcal{P}\bar{v}_s \mathbf{r} \left[\frac{-1}{r^3} + 3 \frac{(\mathbf{r}\cdot\mathbf{p})^2}{r^5} \right]$. Here \mathcal{P} is the dimensionless force–dipole strength normalized by $8\pi\mu a^2 v_s$, which depends on the swimming mechanism^{56–58}. Earlier studies on *E. coli*^{56,58,59} and *Chlamydomonas*⁶⁰ suggest that $|\mathcal{P}|$ varies roughly between 0.04 and 0.3.

The slow decay of the force–dipole field ($\sim 1/r^2$) suggests that the swimming lift obtained from singular perturbation now also is linear in Re_p as the lift evaluated within regular perturbation theory (see Supplementary Note 2). Thus, similar to the case of passive inertial lift^{37,45}, one can use either regular perturbation theory or matched asymptotic expansions to calculate the swimming lift in leading order of Re_p . A comparison of results from singular perturbation approach of Asmolov⁴⁵ and results using regular perturbation theory³⁷, which strictly requires a channel Reynolds number $\text{Re}_c \ll 1$, shows a close match of the lift-force profiles at $\text{Re}_c = 15$ (see Fig. 8 in⁴⁵). This suggests a smooth transition between the two approaches. Therefore, we continue with the approach used for neutral microswimmers and employ regular perturbation theory in combination with the reciprocal theorem in Eq. 3, as detailed in the Supplementary Note 3. The slower decay of the force–dipole field poses an additional challenge: one has to account for the finite integration domain of the microchannel, otherwise the lift would diverge logarithmically. Thus, we correct the zeroth-order flow field \mathbf{v}_0 by including wall terms, which we obtain from the method of reflections. Our investigation shows that the angular dependence of the force–dipole swimming lift, $\mathcal{F}_{\text{swim}} \propto \sin 2\psi$, differs from that of the source dipole. Fitting the numerical results for $\mathcal{F}_{\text{swim}}$, we can approximate the total

inertial lift velocity in units of v_s by

$$\mathcal{F} = \text{Re}_p \left[\kappa \bar{v}_m x \left(1 - \frac{x^2}{x_{\text{eq}}^2} \right) + \mathcal{P} (1 - 2x^2) \sin 2\psi / 2 \right].$$

In Fig. 5a, the lift-velocity profile for a force dipole shows a clear difference to the profile in Fig. 2. Compared to the passive lift ($\psi = 0, \pi/2$), the profile either shifts up or down for varying ψ . Thus, depending on \mathcal{P} and $\bar{v}_m \kappa$, the fixed point ($\mathcal{F} = 0$) in one channel half can vanish completely. We note that the profiles of force dipoles with the same strength but opposite signs follow from each other by adding $\pi/2$ to ψ .

Although the fixed points are identical to the previous case, the stability analysis with the eigenvalues

$$\lambda_1 \approx \frac{\text{Re}_p}{2} \kappa \bar{v}_m \pm i \bar{v}_m^{1/2} \quad \text{and} \quad \lambda_2 \approx \frac{\text{Re}_p}{2} \kappa \bar{v}_m \pm \bar{v}_m^{1/2}.$$

reveals that upstream swimming ($\psi = 0$) is always unstable, as suggested by the lift velocity. Through an unstable spiral, the trajectories enter a stable limit cycle, which for lower flow rates corresponds to a swinging motion about the centerline. The swimmer effectively swims upstream for $\bar{v}_m < 1$ as depicted in Fig. 5b, while it moves downstream for $\bar{v}_m > 1$, similar to the black trajectory in Fig. 3e.

Hydrodynamic wall interactions of the force–dipole field add weak modifications of the order of κ^2 and κ^3 to the evolution equations of position and orientation, respectively^{16,61–63}. Therefore, they mainly influence the dynamics when the flow rates are weak, i.e., for upstream swinging motion. Figure 5c shows a pusher approaching the wall as the hydrodynamic interactions are attractive⁵⁶. Since the strong vorticity near the walls re-orientates the swimmer, it will ultimately oscillate between both walls. In contrast, pullers are hydrodynamically repelled from walls¹⁶ and hence swim in a swinging limit cycle with an amplitude smaller compared to Fig. 5b. Finally, Fig. 5d shows that downstream swinging in stronger flows is hardly affected. For neutral swimmers, the wall effects are weaker by an additional factor of κ ^{62–65} and we verified that they do not have a significant effect on the dynamics.

In Fig. 6a, b we show the resulting state diagrams for a puller and pusher, respectively. The diagrams are clearly disparate to that of a neutral swimmer (Fig. 3a). For flow rates \bar{v}_m below one, larger pullers swim upstream along the centerline (region I) since hydrodynamic wall interactions dominate the inertial lift and push pullers to the center. Otherwise, pushers and pullers show upstream swinging (region II) and for $\bar{v}_m > 1$ downstream swinging (region III). At even larger \bar{v}_m they transition into the tumbling state (region IV). For pushers, this transition occurs at larger \bar{v}_m due to the hydrodynamic wall interactions. Finally, in

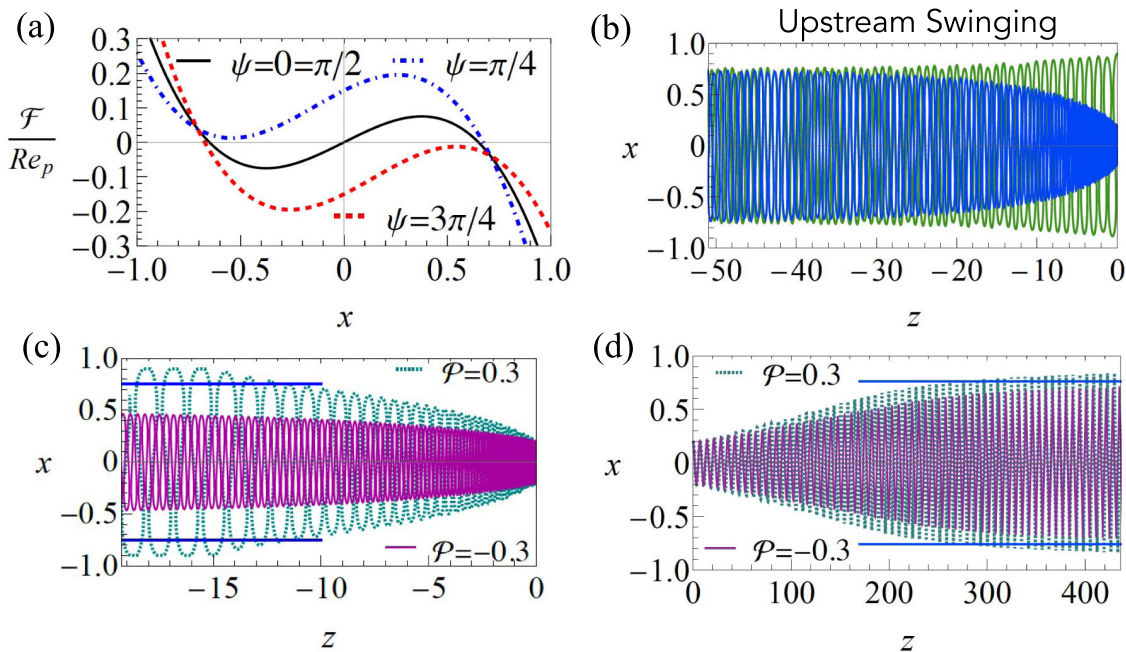


Fig. 5 Lift-velocity profile and dynamics of a force-dipole swimmer. **a** Inertial lift-velocity profile of a pusher ($\mathcal{P} = 0.3$) with $\kappa = 0.1$, $x_{eq} = \pm 0.65$, and $\bar{v}_m = 3$. **b** Upstream swinging trajectories for $\bar{v}_m = 1$. The bottom row shows hydrodynamic wall effects on the upstream and downstream motion of a pusher ($\mathcal{P} = 0.3$) and puller ($\mathcal{P} = -0.3$): **c** $\bar{v}_m = 1$, **d** $\bar{v}_m = 3$. The solid blue line depicts the limit cycle amplitude of **(b)**. $Re_p = 0.1$ is used in all figures.

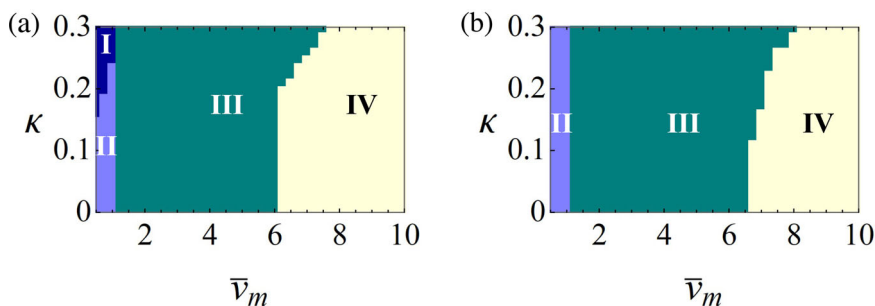


Fig. 6 State diagram of a force-dipole swimmer. Particle size κ versus flow speed \bar{v}_m for **a** puller ($\mathcal{P} = -0.3$) and **b** Pusher ($\mathcal{P} = 0.3$) at $Re_p = 0.1$. Regions I: centerline upstream swimming, II: upstream swinging, III: downstream swinging, and IV: tumbling.

Supplementary Note 4, we provide the time period of the oscillatory states and the axial drift speed as a function of \bar{v}_m for pusher and puller with $\mathcal{P} = \pm 0.3$. Note that at zero Re_p with hydrodynamic wall interactions included, the swimmer states realized at a specific flow speed \bar{v}_m differ from that in Fig. 6. For sufficiently large \bar{v}_m pushers always show stable swinging around the center line, while pullers either move along the centerline or tumble close to the wall depending on their initial conditions¹⁶.

Conclusions

In summary, we have studied how swimming at low fluid inertia in Poiseuille flow adds a swimming lift to the known passive inertial lift velocity. We have concentrated on the generic source-dipole and force-dipole microswimmers and showed that their swimming lift velocities depend differently on the lateral swimmer position and orientation. This gives rise to the emergence of complex dynamics including bistable states, where tumbling coexists with stable centerline swimming or swinging. The Reynolds number determines the overall dynamics relative to the flow speed. Deriving a non-linear oscillator equation for ψ in full analogy to ref.¹⁶, reveals a reduced relaxation time $\propto Re_p^{-1}$ towards the stationary states.

Recent experimental studies^{14,20,57,66} operate within the parameter ranges of microswimmer size, 10–200 μm , and channel width, 100–500 μm . Thus for the maximum flow speed $v_m \sim 1$ mm/s, Re_p ranges from 0.001 to 0.1 and the time taken to attain steady states, $w/(v_s Re_p)$, roughly varies from 10 to 10^3 s for narrow microchannels. These estimates suggest that effects of fluid inertia are observable for large microswimmers ($\gtrsim 50 \mu\text{m}$) and moderate to strong flows. For instance, *Volvox carteri* will be of interest as it has a radius of $\sim 200 \mu\text{m}$ and swims with $\sim 200 \mu\text{m/s}$ ⁵⁷. Additionally, artificial microswimmers with tunable high speeds larger than 200 $\mu\text{m/s}$ exist^{9,30,31}. All this should offer the possibility to experimentally observe the dynamic features reported here at small but non-negligible fluid inertia depending on the hydrodynamic signature of a microswimmer. Furthermore, the current insights may encourage investigations in marine ecosystem, where recent literature^{67,68} suggests that inertial lift can drive planktons out of the turbulent eddies and induce plankton blooms.

Our work extends the research on microswimmers by bringing the role of fluid inertia into focus, which has not been looked at so far. For passive particles, this has spawned the field of inertial microfluidics^{34,35}. We envisage a similar development for microswimmers, which offers numerous aspects to look at. For example, elongated microswimmers perform Jeffery orbits⁶⁹,

which also influence their dynamics in a Poiseuille flow¹⁷. Adding them to the current work is not straightforward since fluid inertia induces an orientational drift⁷⁰. The hydrodynamics of the swimming motion might also add an active component to the Jeffery orbits. We also stress that thermal or biological noise acting on the swimmer orientation will disturb the motion in the limit cycles and also induce transitions between coexisting states but not influence the principal behavior outlined in this article. Finally, we note that incorporation of higher-order multipoles can provide rich dynamical behavior near the walls in the presence of inertia⁷¹.

Methods

Problem formulation. To evaluate the lift velocities, we work in reference frame that translates with the swimmer $(\bar{x}, \bar{y}, \bar{z})$. Supplementary Note 1 and Supplementary Fig. 1 show the non-dimensional notation, where $s = d/2w$ and $s/\kappa = d/a$ denotes the dimensionless distance from the bottom wall in units of particle radius a . For simplicity, we temporarily drop the tilde notation. We divide the full velocity field $\mathbf{v}_{\text{actual}} = \mathbf{v} + \mathbf{v}^\infty$ into the background flow field \mathbf{v}^∞ and the disturbance field \mathbf{v} , and then obtain the equations governing the disturbance field from the continuity and Navier–Stokes equations:

$$\nabla \cdot \mathbf{v} = 0, \quad \text{Re}_p (\mathbf{v}^\infty \cdot \nabla \mathbf{v} + \mathbf{v} \cdot \nabla \mathbf{v}^\infty + \mathbf{v} \cdot \nabla \mathbf{v}) = -\nabla p + \nabla^2 \mathbf{v}. \quad (7)$$

The hydrodynamic equations follow a quasi-steady description as the time scale associated with swimming ($a/v_s \sim 1$ s) is much larger than the characteristic vortex diffusion time ($a^2/\nu \sim 10^{-4}$ s). The above equations have been non-dimensionalized using $a, \kappa v_m, \mu \kappa v_m/a$ as the characteristic scales for length, velocity, and pressure, respectively. The definitions of these dimensional parameters a (particle size), $\kappa = a/2w$, and v_m (maximum flow velocity) are consistent with the article. In our case, \mathbf{v}^∞ is the undisturbed Poiseuille flow velocity in the frame of reference translating/co-moving with the particle

$$\mathbf{v}^\infty = (\alpha + \beta x + \gamma x^2) \mathbf{e}_z - \mathbf{U}_p, \quad (8)$$

where \mathbf{U}_p is the total velocity of the swimmer, i.e., swimming velocity \mathbf{v}_s plus advection due to the Poiseuille flow and the lift velocities. The constants α, β , and γ are:

$$\alpha = 4s(1-s)/\kappa, \quad \beta = 4(1-2s), \quad \gamma = -4\kappa, \quad (9)$$

where β and γ represent the shear and curvature of the background flow, respectively.

The boundary conditions of the disturbance field are:

$$\mathbf{v} = \mathbf{v}_\theta + \boldsymbol{\Omega}_s \times \mathbf{r} - \mathbf{v}^\infty \quad \text{at } r = 1, \quad (10a)$$

$$\mathbf{v} = 0 \quad \text{at walls}, \quad (10b)$$

$$\mathbf{v} \rightarrow \mathbf{0} \quad \text{as } \{y, z\} \rightarrow \infty. \quad (10c)$$

Here, the walls are located at $x = -s/\kappa$ and $x = (1-s)/\kappa$, and \mathbf{v}_θ represents the prescribed tangential surface velocity of the spherical microswimmer.

We find the inertial lift or migration velocities at $O(\text{Re}_p)$ using a regular perturbation expansion. For small values of Re_p , the disturbance field variables are expanded as:

$$\xi = \xi_0 + \text{Re}_p \xi_1 + \dots \quad (11)$$

Here, ξ is a generic field variable that represents velocity (\mathbf{v}), pressure (p), translational (\mathbf{U}_p), and angular velocity ($\boldsymbol{\Omega}_p$). We substitute (11) in the equations governing the disturbance field (7), and obtain the problem at $O(1)$ (i.e. Stokes problem) as

$$\left. \begin{aligned} \nabla \cdot \mathbf{v}_0 &= 0, \\ \nabla^2 \mathbf{v}_0 - \nabla p_0 &= \mathbf{0}, \\ \mathbf{v}_0 &= \mathbf{v}_\theta + \boldsymbol{\Omega}_{p0} \times \mathbf{r} - \mathbf{v}_0^\infty \quad \text{at } r = 1, \\ \mathbf{v}_0 &= 0 \quad \text{at walls}, \\ \mathbf{v}_0 &\rightarrow \mathbf{0} \quad \text{as } \{y, z\} \rightarrow \infty, \end{aligned} \right\} \quad (12)$$

and at $O(\text{Re}_p)$ as:

$$\left. \begin{aligned} \nabla \cdot \mathbf{v}_1 &= 0, \\ \nabla^2 \mathbf{v}_1 - \nabla p_1 &= (\mathbf{v}_0^\infty \cdot \nabla \mathbf{v}_0 + \mathbf{v}_0 \cdot \nabla \mathbf{v}_0^\infty + \mathbf{v}_0 \cdot \nabla \mathbf{v}_0), \\ \mathbf{v}_1 &= \mathbf{U}_{p1} + \boldsymbol{\Omega}_{p1} \times \mathbf{r} \quad \text{at } r = 1, \\ \mathbf{v}_1 &= \mathbf{0} \quad \text{at walls}, \\ \mathbf{v}_1 &\rightarrow \mathbf{0} \quad \text{as } \{y, z\} \rightarrow \infty. \end{aligned} \right\} \quad (13)$$

In (12), $\mathbf{v}_0^\infty = (\alpha + \beta x + \gamma x^2) \mathbf{e}_z - \mathbf{U}_{p0}$.

Ho and Leal³⁷, in their seminal work, used the reciprocal theorem to derive a volume integral expression for the migration velocity associated with the

$O(\text{Re}_p)$ Eq. 13:

$$-\frac{\text{Re}_p}{6\pi} \int_{V_f} \mathbf{u}^t \cdot (\mathbf{v}_0^\infty \cdot \nabla \mathbf{v}_0 + \mathbf{v}_0 \cdot \nabla \mathbf{v}_0^\infty + \mathbf{v}_0 \cdot \nabla \mathbf{v}_0) dV. \quad (14)$$

The auxiliary or test field (\mathbf{v}^t, p^t) is associated with a sphere moving in the positive x -direction (towards the upper wall) with unit velocity in a quiescent fluid:

$$\mathbf{v}^t(\mathbf{r}) = \frac{3}{4} \left(\mathbf{e}_x + \frac{x\mathbf{r}}{r^2} \right) \frac{1}{r} + \frac{1}{4} \left(\mathbf{e}_x - \frac{3x\mathbf{r}}{r^2} \right) \frac{1}{r^3}. \quad (15)$$

The reciprocal theorem makes it relatively easy to find lift velocities at $O(\text{Re}_p)$, as we can solve the creeping flow problem (12) using well-established methods^{61,72} and directly substitute its solution in (14). In other words, we do not need to solve the $O(\text{Re}_p)$ problem (13) to obtain the $O(\text{Re}_p)$ lift.

Lift velocity. We now use the reciprocal theorem integral (14) for evaluating the swimming lift of a source–dipole swimmer. We explicitly choose the axisymmetric neutral squirmer, which has the surface velocity field $\mathbf{v}_\theta = B_1 \sin \theta \mathbf{e}_\theta$, where θ is the polar angle and \mathbf{e}_θ the corresponding base vector. The swimming velocity is directly related to this squirmer coefficient: $v_s = 2B_1/3^{52,73}$. The solution to the $O(1)$ Stokes problem (12) in the Poiseuille background flow is obtained as (4). The first part in the above expression is the swimmer-generated source–dipole, and the second part is the stresslet and the higher-order octupole correction due to the local shear flow⁷⁴. \mathbf{e}^∞ is the rate of strain tensor for the background flow, which amounts to $\mathbf{e}^\infty = (\nabla \mathbf{v}^\infty + \nabla \mathbf{v}^{\infty \dagger})/2$ (here \dagger represents transpose). For the case of a small neutral swimmer, we can neglect the curvature of the background flow, that would bring in a term proportional to $\gamma \sim O(\kappa)$ in Eq. 4. Additionally, the previous work⁴¹ suggests that the hydrodynamic multipoles arising from the curvature have a negligible effect on the lift of a source–dipole swimmer.

It remains to calculate \mathbf{e}^∞ for the Poiseuille flow of Eq. 8 in zeroth order of Re_p . The total velocity of the force-free swimmer in the Stokes regime is $\mathbf{U}_{p0} = \bar{\mathbf{v}}_s + \alpha \mathbf{e}_z$, where the second part is obtained by the fact that the swimmer at $x = 0$ is advected by the flow. To complete the expression of \mathbf{v}_0^∞ , we substitute \mathbf{U}_{p0} in (8), and obtain:

$$\mathbf{v}_0^\infty = (\beta x) \mathbf{e}_z - \bar{\mathbf{v}}_s, \quad (16)$$

which gives $[\mathbf{e}^\infty]_{xz} = [\mathbf{e}^\infty]_{zx} = \beta/2$.

Now, we evaluate the lift integral arising from the active nature of the swimmer (in addition to the passive lift). Since the source–dipole field of the neutral swimmer decays quickly away from the swimmer ($\sim 1/r^3$), we can neglect the wall corrections in the lift velocity integral (14). In the context of electrophoresis, Choudhary et al.⁴¹ showed that accounting for such wall corrections hardly affects the lift and only becomes noticeable very near the walls (see⁴¹, p. 877). That work also showed that higher-order effects due to curvature are negligible in the case of a source dipole⁴¹, p. 879. Hence, we evaluate the lift velocity integral by substituting (16) and (4) in (14). Integrating over the infinite space, we obtain the swimming lift velocity in units of v_s as

$$\mathcal{F}_{\text{swim}} = (7/24) \text{Re}_p \beta \cos \psi, \quad (17)$$

expressed in the co-moving frame of the swimmer. See Supplementary Software 1 for the details of evaluation. In Eq. 17 the contribution from the disturbance–disturbance interaction term of the integral ($\mathbf{v}_0 \cdot \nabla \mathbf{v}_0$) is $(49/360) \text{Re}_p \beta \cos \psi$ and the contribution arising from the disturbance–flow interaction term ($\mathbf{v}_0^\infty \cdot \nabla \mathbf{v}_0 + \mathbf{v}_0 \cdot \nabla \mathbf{v}_0^\infty$) is $(7/45) \text{Re}_p \beta \cos \psi$. Note, to calculate the passive inertial lift, one must account for wall interactions and the curvature γ in \mathbf{v}_0^∞ .

For a force–dipole swimmer, we obtain the lift velocity in the units of v_s as:

$$\mathcal{F}_{\text{swim}} \approx 0.5 \text{Re}_p \mathcal{P} [-1 + 8(s - s^2)] \sin 2\psi. \quad (18)$$

The evaluation is detailed in Supplementary Note 3. Supplementary Fig. 2 shows fits for the swimming–lift profile of a pusher.

The final expressions of the swimming and passive lift velocities in the channel frame of reference can be obtained by a transformation of particle–wall distance s to the channel x coordinate: $s = (1+x)/2$. Using the definition of β from Eq. 9, Eq. 17 is obtained as $-(7/6) \text{Re}_p x \cos \psi$. Similarly, we obtain the swimming lift velocity of a force–dipole swimmer as $0.5 \text{Re}_p \mathcal{P} (1 - 2x^2) \sin 2\psi$.

Following the prior works on inertial migration^{37,41,75}, we reproduce the lift force profile for a passive neutrally buoyant particle suspended in Poiseuille flow, which needs the numerical evaluation of integrals. Supplementary Fig. 3 shows the comparison of our reproduced results for passive lift with Vasseur and Cox⁷⁵ and also illustrates the fitted function used in the article:

$$\mathcal{F}_{\text{passive}} = \text{Re}_p \kappa \bar{v}_m x \left(1 - \frac{x^2}{x_{eq}^2} \right). \quad (19)$$

Data availability

Data sharing not applicable to this article as no datasets were generated or analyzed during the current study.

Code availability

Supplementary Software 1 files include a Mathematica code for the results.

Received: 9 September 2021; Accepted: 17 December 2021;

Published online: 11 January 2022

References

- Levy, R., Hill, D. B., Forest, M. G. & Grotberg, J. B. Pulmonary fluid flow challenges for experimental and mathematical modeling. *Integr. Comp. Biol.* **54**, 985–1000 (2014).
- Bhattacharjee, T. & Datta, S. S. Bacterial hopping and trapping in porous media. *Nat. Commun.* **10**, 1–9 (2019).
- Riffell, J. A. & Zimmer, R. K. Sex and flow: The consequences of fluid shear for sperm–egg interactions. *J. Exp. Bio.* **210**, 3644–3660 (2007).
- Schaar, K., Zöttl, A. & Stark, H. Detention times of microswimmers close to surfaces: Influence of hydrodynamic interactions and noise. *Phys. Rev. Lett.* **115**, 038101 (2015).
- Daddi-Moussa-Ider, A., Löwen, H. & Liebchen, B. Hydrodynamics can determine the optimal route for microswimmer navigation. *Commun. Phys.* **4**, 1–11 (2021).
- Conrad, J. C. & Poling-Skutvik, R. Confined flow: consequences and implications for bacteria and biofilms. *Annu. Rev. Chem. Biomol. Eng.* **9**, 175–200 (2018).
- Rühle, F. & Stark, H. Emergent collective dynamics of bottom-heavy squirmers under gravity. *Eur. Phys. J. E* **43**, 1–17 (2020).
- Nelson, B. J. & Peyer, K. E. Micro-and nanorobots swimming in heterogeneous liquids. *ACS Nano* **8**, 8718–8724 (2014).
- Zhou, H., Mayorga-Martinez, C. C., Pané, S., Zhang, L. & Pumerá, M. Magnetically driven micro and nanorobots. *Chem. Rev.* **121**, 4999–5041 (2021).
- Peng, Z. & Brady, J. F. Upstream swimming and Taylor dispersion of active Brownian particles. *Phys. Rev. Fluids* **5**, 073102 (2020).
- Rusconi, R., Lecuyer, S., Guglielmini, L. & Stone, H. A. Laminar flow around corners triggers the formation of biofilm streamers. *J. R. Soc. Interface* **7**, 1293–1299 (2010).
- Hill, J., Kalkanci, O., McMurry, J. L. & Koser, H. Hydrodynamic surface interactions enable *Escherichia coli* to seek efficient routes to swim upstream. *Phys. Rev. Lett.* **98**, 068101 (2007).
- Nash, R., Adhikari, R., Tailleux, J. & Cates, M. Run-and-tumble particles with hydrodynamics: Sedimentation, trapping, and upstream swimming. *Phys. Rev. Lett.* **104**, 258101 (2010).
- Tung, C.-k. et al. Emergence of upstream swimming via a hydrodynamic transition. *Phys. Rev. Lett.* **114**, 108102 (2015).
- Mathijssen, A. J. et al. Oscillatory surface rheotaxis of swimming *e. coli* bacteria. *Nat. Commun.* **10**, 1–12 (2019).
- Zöttl, A. & Stark, H. Nonlinear dynamics of a microswimmer in poiseuille flow. *Phys. Rev. Lett.* **108**, 218104 (2012).
- Zöttl, A. & Stark, H. Periodic and quasiperiodic motion of an elongated microswimmer in Poiseuille flow. *Eur. Phys. J. E* **36**, 1–10 (2013).
- Uppaluri, S. et al. Flow loading induces oscillatory trajectories in a bloodstream parasite. *Biophys. J.* **103**, 1162–1169 (2012).
- Junot, G., Clément, E., Auradou, H. & García-García, R. Single-trajectory characterization of active swimmers in a flow. *Phys. Rev. E* **103**, 032608 (2021).
- Rusconi, R., Guasto, J. S. & Stocker, R. Bacterial transport suppressed by fluid shear. *Nat. Phys.* **10**, 212–217 (2014).
- García, X., Rafai, S. & Peyla, P. Light control of the flow of phototactic microswimmer suspensions. *Phys. Rev. Lett.* **110**, 138106 (2013).
- Waisbord, N., Lefèvre, C. T., Bocquet, L., Ybert, C. & Cottin-Bizonne, C. Destabilization of a flow focused suspension of magnetotactic bacteria. *Phys. Rev. Fluids* **1**, 053203 (2016).
- Meng, F., Matsunaga, D. & Golestanian, R. Clustering of magnetic swimmers in a Poiseuille flow. *Phys. Rev. Lett.* **120**, 188101 (2018).
- Wang, S. & Ardekani, A. Unsteady swimming of small organisms. *J. Fluid Mech.* **702**, 286 (2012).
- Hamel, A., Fisch, C., Combettes, L., Dupuis-Williams, P. & Baroud, C. N. Transitions between three swimming gaits in paramecium escape. *Proc. Natl Acad. Sci. USA* **108**, 7290–7295 (2011).
- Wang, S. & Ardekani, A. Inertial squirmers. *Phys. Fluids* **24**, 101902 (2012).
- Khair, A. S. & Chisholm, N. G. Expansions at small Reynolds numbers for the locomotion of a spherical squirmer. *Phys. Fluids* **26**, 011902 (2014).
- Scholz, C., Jahanshahi, S., Ldov, A. & Löwen, H. Inertial delay of self-propelled particles. *Nat. Commun.* **9**, 1–9 (2018).
- Löwen, H. Inertial effects of self-propelled particles: From active Brownian to active Langevin motion. *J. Chem. Phys.* **152**, 040901 (2020).
- Ren, L. et al. 3d steerable, acoustically powered microswimmers for single-particle manipulation. *Sci. Adv.* **5**, 3084 (2019).
- Aghakhani, A., Yasa, O., Wrede, P. & Sitti, M. Acoustically powered surface-slipping mobile microrobots. *Proc. Natl Acad. Sci. USA* **117**, 3469–3477 (2020).
- Segre, G. & Silberberg, A. Radial particle displacements in Poiseuille flow of suspensions. *Nature* **189**, 209 (1961).
- Segre, G. & Silberberg, A. Behaviour of macroscopic rigid spheres in Poiseuille flow part 2. Experimental results and interpretation. *J. Fluid Mech.* **14**, 136–157 (1962).
- Di Carlo, D. Inertial microfluidics. *Lab Chip* **9**, 3038–3046 (2009).
- Zhang, J. et al. Fundamentals and applications of inertial microfluidics: A review. *Lab Chip* **16**, 10–34 (2016).
- Batchelor, G. *An Introduction to Fluid Dynamics* (Cambridge University Press, 1967).
- Ho, B. & Leal, L. Inertial migration of rigid spheres in two-dimensional unidirectional flows. *J. Fluid Mech.* **65**, 365–400 (1974).
- Saffman, P. The lift on a small sphere in a slow shear flow. *J. Fluid Mech.* **22**, 385–400 (1965).
- Kim, Y. W. & Yoo, J. Y. Axisymmetric flow focusing of particles in a single microchannel. *Lab Chip* **9**, 1043–1045 (2009).
- Yuan, D. et al. Tunable particle focusing in a straight channel with symmetric semicircle obstacle arrays using electrophoresis-modified inertial effects. *Micromachines* **7**, 195 (2016).
- Choudhary, A., Renganathan, T. & Pushpavanam, S. Inertial migration of an electrophoretic rigid sphere in a two-dimensional Poiseuille flow. *J. Fluid Mech.* **874**, 856–890 (2019).
- Khair, A. S. & Kabarowski, J. K. Migration of an electrophoretic particle in a weakly inertial or viscoelastic shear flow. *Phys. Rev. Fluids* **5**, 033702 (2020).
- Choudhary, A., Renganathan, T. & Pushpavanam, S. Comment on: Migration of an electrophoretic particle in a weakly inertial or viscoelastic shear flow. *Phys. Rev. Fluids* **6**, 036701 (2021).
- Schonberg, J. A. & Hinch, E. Inertial migration of a sphere in poiseuille flow. *J. Fluid Mech.* **203**, 517–524 (1989).
- Asmolov, E. S. The inertial lift on a spherical particle in a plane Poiseuille flow at large channel Reynolds number. *J. Fluid Mech.* **381**, 63–87 (1999).
- Evans, A. A., Ishikawa, T., Yamaguchi, T. & Lauga, E. Orientational order in concentrated suspensions of spherical microswimmers. *Phys. Fluids* **23**, 111702 (2011).
- Thutupalli, S., Seemann, R. & Herminghaus, S. Swarming behavior of simple model squirmers. *N. J. Phys.* **13**, 073021 (2011).
- Schmitt, M. & Stark, H. Active Brownian motion of emulsion droplets: Coarsening dynamics at the interface and rotational diffusion. *Eur. Phys. J. E* **39**, 1–15 (2016).
- Oseen, C. W. About Stokes' formula and a related problem in hydrodynamics. *Ark. Mat., Astron. Phys.* **6**, 1 (1910).
- Lighthill, M. On the squirming motion of nearly spherical deformable bodies through liquids at very small Reynolds numbers. *Commun. Pure Appl. Math.* **5**, 109–118 (1952).
- Blake, J. R. A spherical envelope approach to ciliary propulsion. *J. Fluid Mech.* **46**, 199–208 (1971).
- Zöttl, A. & Stark, H. Emergent behavior in active colloids. *J. Phys.: Condens. Matter* **28**, 253001 (2016).
- Strogatz, S. H. *Nonlinear Dynamics and Chaos: With Applications to Physics, Biology, Chemistry, and Engineering* (CRC Press, 2018).
- Perko, L. *Differential Equations and Dynamical Systems* Vol. 7 (Springer Science & Business Media, 2013).
- Pedley, T. & Kessler, J. O. Hydrodynamic phenomena in suspensions of swimming microorganisms. *Annu. Rev. Fluid Mech.* **24**, 313–358 (1992).
- Berke, A. P., Turner, L., Berg, H. C. & Lauga, E. Hydrodynamic attraction of swimming microorganisms by surfaces. *Phys. Rev. Lett.* **101**, 038102 (2008).
- Drescher, K., Goldstein, R. E., Michel, N., Polin, M. & Tuval, I. Direct measurement of the flow field around swimming microorganisms. *Phys. Rev. Lett.* **105**, 168101 (2010).
- Drescher, K., Dunkel, J., Cisneros, L. H., Ganguly, S. & Goldstein, R. E. Fluid dynamics and noise in bacterial cell–cell and cell–surface scattering. *Proc. Natl Acad. Sci. USA* **108**, 10940–10945 (2011).
- Chattopadhyay, S., Moldovan, R., Yeung, C. & Wu, X. Swimming efficiency of bacterium *Escherichiacoli coli*. *Proc. Natl Acad. Sci. USA* **103**, 13712–13717 (2006).
- Minoura, I. & Kamiya, R. Strikingly different propulsive forces generated by different dynein-deficient mutants in viscous media. *Cell Motil. Cytoskeleton* **31**, 130–139 (1995).
- Kim, S. & Karrila, S. J. *Microhydrodynamics: Principles and Selected Applications* (Courier Corporation, 2013).
- Ibrahim, Y. & Liverpool, T. B. How walls affect the dynamics of self-phoretic microswimmers. *Eur. Phys. J. Spec. Top.* **225**, 1843–1874 (2016).
- Shaik, V. A. & Ardekani, A. M. Motion of a model swimmer near a weakly deforming interface. *J. Fluid Mech.* **824**, 42 (2017).

64. Spagnolie, S. E. & Lauga, E. Hydrodynamics of self-propulsion near a boundary: Predictions and accuracy of far-field approximations. *J. Fluid Mech.* **700**, 105–147 (2012).
65. Choudhary, A., Chaithanya, K., Michelin, S. & Pushpavanam, S. Self-propulsion in 2d confinement: phoretic and hydrodynamic interactions. *Eur. Phys. J. E* **44** 7, 97 (2021).
66. Barry, M. T., Rusconi, R., Guasto, J. S. & Stocker, R. Shear-induced orientational dynamics and spatial heterogeneity in suspensions of motile phytoplankton. *J. R. Soc. Interface* **12**, 20150791 (2015).
67. Woodward, J. R., Pitchford, J. W. & Bees, M. A. Physical flow effects can dictate plankton population dynamics. *J. R. Soc. Interface* **16**, 20190247 (2019).
68. Beron-Vera, F. J. Nonlinear dynamics of inertial particles in the ocean: From drifters and floats to marine debris and sargassum. *Nonlinear Dyn.* **103**, 1–26 (2021).
69. Jeffery, G. B. The motion of ellipsoidal particles immersed in a viscous fluid. *Proc. Math. Phys. Eng.* **102**, 161–179 (1922).
70. Einarsson, J., Candelier, F., Lundell, F., Angilella, J. & Mehlig, B. Rotation of a spheroid in a simple shear at small Reynolds number. *Phys. Fluids* **27**, 063301 (2015).
71. Lintuvuori, J. S., Brown, A. T., Stratford, K. & Marenduzzo, D. Hydrodynamic oscillations and variable swimming speed in squirmers close to repulsive walls. *Soft Matter* **12**, 7959–7968 (2016).
72. Lamb, H. *Hydrodynamics* 6th edn (Cambridge University Press, 1975).
73. Ishikawa, T., Simmonds, M. & Pedley, T. J. Hydrodynamic interaction of two swimming model micro-organisms. *J. Fluid Mech.* **568**, 119–160 (2006).
74. Guazzelli, E. & Morris, J. F. *A Physical Introduction to Suspension Dynamics* Vol. 45 (Cambridge University Press, 2011).
75. Vasseur, P. & Cox, R. The lateral migration of a spherical particle in two-dimensional shear flows. *J. Fluid Mech.* **78**, 385–413 (1976).

Acknowledgements

Support from the Alexander von Humboldt Foundation is gratefully acknowledged. We also acknowledge financial support from the Collaborative Research Center 910 funded by the Deutsche Forschungsgemeinschaft.

Author contributions

A.C., F.R., and H.S. planned the research. A.C., F.R., and S.P. performed the calculations. A.C. and H.S. wrote the manuscript.

Funding

Open Access funding enabled and organized by Projekt DEAL.

Competing interests

The authors declare no competing interests.

Additional information

Supplementary information The online version contains supplementary material available at <https://doi.org/10.1038/s42005-021-00794-y>.

Correspondence and requests for materials should be addressed to Akash Choudhary or Holger Stark.

Peer review information *Communications Physics* thanks Shiyang Wang and the other, anonymous, reviewer(s) for their contribution to the peer review of this work.

Reprints and permission information is available at <http://www.nature.com/reprints>

Publisher's note Springer Nature remains neutral with regard to jurisdictional claims in published maps and institutional affiliations.



Open Access This article is licensed under a Creative Commons Attribution 4.0 International License, which permits use, sharing, adaptation, distribution and reproduction in any medium or format, as long as you give appropriate credit to the original author(s) and the source, provide a link to the Creative Commons license, and indicate if changes were made. The images or other third party material in this article are included in the article's Creative Commons license, unless indicated otherwise in a credit line to the material. If material is not included in the article's Creative Commons license and your intended use is not permitted by statutory regulation or exceeds the permitted use, you will need to obtain permission directly from the copyright holder. To view a copy of this license, visit <http://creativecommons.org/licenses/by/4.0/>.

© The Author(s) 2022